Composites Science and Technology 218 (2022) 109141

Contents lists available at ScienceDirect

Composites Science and Technology

journal homepage: www.elsevier.com/locate/compscitech

Failure prediction for high-strain rate and out-of-plane compression of fibrous composites

Nazanin Pournoori *, Oscar Rodera, Jarno Jokinen, Mikko Hokka, Mikko Kanerva

Engineering Materials Science, Faculty of Engineering and Natural Sciences, Tampere University, POB 33014, Tampere, Finland

ARTICLE INFO

Keywords:
High strain rate
Glass fibers
Fracture
Failure criterion
Finite element analysis (FEA)

ABSTRACT

This work presents a detailed analysis of failure prediction for a glass fiber reinforced plastic (GFRP) composite under out-of-plane compression at quasi-static (10^{-3} and 1 s^{-1}) and high strain rates (10^{3} s^{-1}). The simulations were compared with the experiments of a recent study (*Pournoori.* et al. *Int. J. Impact Eng., 147 (2021)*). The failure at different strain rates was predicted using the three-dimensional (3D) Hashin failure criterion implemented into the finite element analysis by the Abaqus user-defined subroutines UMAT and VUMAT. According to the results, the criterion predicted failure onset well in terms of force level, location, and failure mode, without any fitting parameters. The inter-fiber failure was the dominant failure mode at all studied strain rates in simulations. The 3D Hashin criterion predicted that the failure onset occurred at a low strain level close to the experimental nonlinearity point with a ±7% difference between them while the coefficient of variation of related strains at nonlinearity point was 15.4% at low and intermediate rate tests. The virtual crack closure technique simulations of fracture for low and high rate tests indicated that the GFRP deformation involves some dissipation, which causes a type of nonlinear response prior to the peak force.

1. Introduction

The failure mechanisms of fibrous composites at high strain rates (above 100 s^{-1}) have been previously studied experimentally, using different test methods, such as servo-hydraulic machines, impact drop-weight system, and the Split Hopkinson Pressure Bar (SHPB) [1,2]. According to these experiments, various failure modes from matrix cracking to delamination have been observed in fiber reinforced polymers (FRPs). In general, the failure modes in composites under either in-plane or out-of-plane loading depend strongly on the fibers' orientation [1]. Okereke et al. [3] found that the dominant failure mechanism is the interlaminar matrix failure for a unidirectional (UD) GFRP under in-plane compression at low, medium, and high rates tests. The onset of macroscopic damage was interpreted by the rapid fall in the stress for the high rate tests [4]. It should be noted that the difficulties inherent to the high rate testing of composites have often led to inconclusive results [5].

Predictive failure criteria for FRPs have been developed for long, and successful criteria have been found for unidirectional plies as well as laminates under in-plane loading at low and intermediate rates [6,7]. Among the FRP failure criteria, the 3D Hashin criterion has been widely used due to its prediction accuracy and ease of use as well as computational efficiency [8]. However, the Hashin criterion is incapable of predicting the increase of the shear strength of a ply under in-plane transverse compression and might not account for the reduction of compressive strength [9,10].

Recently, the strain rate dependent failure criteria have been developed to study the failure envelopes as well as failure modes in composites, essentially for in-plane compression [11–13]. Damage and its evolution have been studied on the basis of constitutive laws and in terms of degradation of stiffness and also viscoplastic behavior under in-plane compression [14–16]. However, the strain rate effects on the location of failure onset and failure stress-strain values in the composite lay-up have been neglected so far. The prediction of failure in composite structures is very complex and depends on the laminate configuration and the direction of impact loading. Therefore, it is not clear if the rate dependent criteria can successfully predict the failure mode and the load level under high rate compression, in the out-of-plane direction.

The studies of failure criteria and their validity, in particular for the out-of-plane high strain rate compressive loading, are very scarce in the current literature. Typically, the damage initiation in GFRP laminates under out-of-plane compression has been observed experimentally using

* Corresponding author.
E-mail address: Nazanin.Pournoori@tuni.fi (N. Pournoori).

https://doi.org/10.1016/j.compscitech.2021.109141
Received 10 June 2021; Received in revised form 1 November 2021; Accepted 6 November 2021
Available online 11 November 2021

the high-speed optical imaging [4,17]. Kara et al. investigated the damage initiation and propagation of a GFRP composite both experimentally and numerically [18]. They considered the average maximum stress as the failure stress in the experiments. The numerical failure stress of the (homogenized) laminate was also determined by fitting the experimental values with the function of logarithmic strain rate dependency. However, the local failure stress/strain was not predicted inside the composite lay-up, and continuum damage mechanics were used to model the crack propagation. The cohesive damage model has been used to simulate the delamination initiation and propagation under in-plane high strain rate compression [13]. However, the presented model did not analyze the ply failure, only the degradation at ply interfaces.

In this work, we focused on the failure of GFRP at a high strain rate by using numerical models and simulations to reveal: 1) the prediction of the internal failure modes in the GFRP lay-up under out-of-plane compressive loading, 2) the exact location of failure onset and the local failure stresses/strains inside individual plies, and 3) the effect of crack tip opening by using the finite element method and fracture mechanics (Virtual Crack Closure Technique (VCCT)). For these purposes, the strain rate dependent stiffness was determined based on the recent experimental data [19]. Then, the 3D Hashin failure criterion was implemented to predict the failure onset locations and modes, by using the quasi-static strength parameters defined prior to the high rate case studies. The agreement of the FEA prediction with the detailed experimental observations in terms of nonlinearity, visible crack onset, and peak force was analyzed for a range of strain rates.

2. Materials and method

2.1. Experimental data

Recently, out-of-plane compression experiments were performed on pultruded (in detail pull-wound) E-glass fiber reinforced polyester composite specimens with a [0°,85°,0°] lay-up at three strain rates: 10^{-3}, 1, and 10^{3} s^{-1} (i.e., low, intermediate, and high strain rate, respectively) [19]. The illustration of the lay-up and laminate's coordinate system are shown in Fig. 1 (a). The low and intermediate strain rate tests were carried out using an Instron 8800 servo-hydraulic testing machine, and the high strain rate tests were carried out with a SHPB. The details of the experimental setup can be found in our recent study [19]. The failure or the damage onset point of the specimen in the experiments was defined to be the point when the crack was visually observed.

2.2. Failure criterion

The 3D Hashin (3DH) failure criterion is able to predict the onset of different failure modes as defined by the following equations [20,21]:

The fiber tensile mode (here simply called fiber failure, FF): ($\sigma_{11} > 0$)

$$\left(\frac{\sigma_{11}}{X_t}\right)^2 + \left(\frac{\sigma_{12}}{S_{xy}}\right)^2 + \left(\frac{\sigma_{13}}{S_{xy}}\right)^2 = 1 \tag{1}$$

The fiber compression mode (here simply called fiber failure, FF): ($\sigma_{11} < 0$)

$$\left(\frac{\sigma_{11}}{X_c}\right)^2 = 1 \tag{2}$$

The matrix tensile mode (here simply called inter-fiber failure, IFF): ($\sigma_{22} + \sigma_{33} > 0$)

$$\frac{1}{Y_t^2}(\sigma_{22}+\sigma_{33})^2 + \frac{1}{S_{xy}^2}\left(\sigma_{12}^2+\sigma_{13}^2\right) + \frac{1}{S_{yz}^2}\left(\sigma_{23}^2-\sigma_{22}\sigma_{33}\right) = 1 \tag{3}$$

The matrix compression mode (here simply called inter-fiber failure, IFF): ($\sigma_{22} + \sigma_{33} < 0$)

$$\frac{1}{Y_c}\left[\left(\frac{Y_c}{2S_{yz}}\right)^2 - 1\right](\sigma_{22}+\sigma_{33}) + \frac{1}{S_{xy}^2}\left(\sigma_{12}^2+\sigma_{13}^2\right) + \frac{1}{4S_{yz}^2}(\sigma_{22}+\sigma_{33})^2 + \frac{1}{S_{yz}^2}\left(\sigma_{23}^2-\sigma_{22}\sigma_{33}\right) = 1 \tag{4}$$

In the equations above, the strength constants are given in Table 1, and the numeral sub-indices refer to the tensorial stress components in the ply's Cartesian (3D) coordinate system. The 3DH was implemented as user-defined subroutines, UMAT and VUMAT.

2.3. Virtual crack closure technique

The prediction of failure propagation in laminates is complicated, and often the cracks are analyzed 'as is' (via singularity). The VCCT is an effective method based on the LEFM principle to determine the energy release rate (ERR) at the crack tip. This method assumes that the energy released by the propagation of a crack is identical to the strain energy required to close the crack. Therefore, the ERR can be calculated using the nodal forces at the crack tip and the relative displacements in the local elements adjacent to the crack tip [22]. For the ERR calculation, a linear power law-type criterion for the mixed-mode fracture was used:

$$\frac{G_I}{G_{IC}} + \frac{G_{II}}{G_{IIC}} + \frac{G_{III}}{G_{IIIC}} = 1 \tag{5}$$

where G is the ERR, the subscript C denotes a 'critical' value and the subscripts I, II, and III refer to different fracture modes.

2.4. Strain rate dependent elasticity

In the SHPB experiment, it takes time for the stress and strain in the specimen to reach an equilibrium; the stress pulse needs to travel back and forth through the specimen at least five to six times [23]. Therefore, it is difficult to obtain an accurate value for the elastic modulus to be used in simulations of high strain rate tests. The well-known rate scaling

Table 1
Material constants of the GFRP determined for quasi-static performance [25].

Engineering constants			Strength constants (MPa)		
$E_1 = 35$ GPa	$G_{12} = 3.6$ GPa	$\nu_{12} = 0.3$	$X_t = 500$	$Y_t = 50$	$Z_t = 50$
$E_2 = 7$ GPa	$G_{13} = 2$ GPa	$\nu_{13} = 0.3$	$X_c = 200$	$Y_c = 100$	$Z_c = 100$
$E_3 = 4.5$ GPa[a]	$G_{23} = 3.6$ GPa	$\nu_{23} = 0.3$[b]	$S_{xy} = 40$	$S_{xz} = 26$	$S_{yz} = 36$

[a] Based on the recent experimental data [19].
[b] A value of 0.4 was also studied.

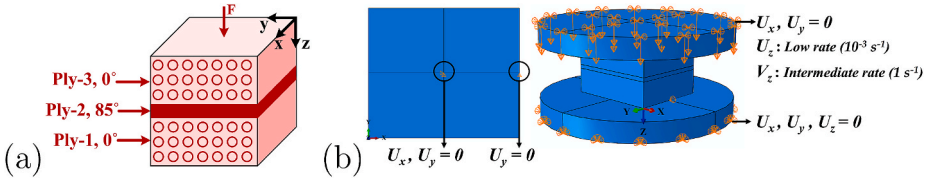

Fig. 1. a) The schematic picture of the test specimen [19] b) the boundary conditions and loading used in the simulation of the quasi-static compression tests.

of (Young's) moduli was used to calculate the high strain rate elastic modulus as [18]:

$$E_{rt} = E_0\left(1 + C\ln\frac{\dot{\varepsilon}}{\dot{\varepsilon}_0}\right) \quad (6)$$

where E_0 is the reference modulus (at low-rate), $\dot{\varepsilon}_0$ is the strain rate of the reference loading, and C is the strain rate sensitivity constant. In this study, the value of C was solved with the logarithmic regression to the experimental data [19] at strain rates of 10^{-3} s^{-1} and 1 s^{-1}. The Young's moduli at the low rate (10^{-3} s^{-1}) and at the intermediate rate (1 s^{-1}) were 4.5 GPa and 9.2 GPa. Finally, the effective modulus in the simulation of the SHPB test at the strain rate of 10^3 s^{-1} was calculated (E_{rt} = 12.35 GPa).

3. Finite element modelling

3D finite element models, for the out-of-plane compression, were created using the Abaqus Standard/Explicit (2017) to study the failure prediction in each of the tested specimens (separate models). The geometry of each specimen was modelled in detail with a cuboid configuration and according to the real dimensions [19]; the failure was predicted independent of the geometry. However, the cubic specimen geometry might indicate a higher stress level than an axisymmetric specimen at the high strain rate – regardless of the type of the tested material [24]. Each specimen model consisted of three plies (using geometry partitions) with different material orientations corresponding to the real lay-up, as shown in Fig. 1 (a).

The engineering constants, listed in Table 1 (for the static case), were used to define anisotropic elastic deformation. The Poisson's ratios of 0.3 and 0.4 were considered in the simulations to study its effects on the failure onset prediction (see supplementary data). The density of the GFRP for the dynamic (explicit) simulation was 1870 kg/m^3. The fully integrated linear hexahedral (C3D8) elements were used. Two different mesh densities were considered to study the applicability of the failure criterion for different modelling resolutions: (1) 0.1 mm in-plane and a single ply-size in the thickness direction; and (2) 0.1 mm (cubic shape, here called the 'dense mesh').

3.1. Simulations of the quasi-static tests (10^{-3} s^{-1} and 1 s^{-1})

The quasi-static tests were modelled including deformable steel anvils, which were placed above and below the specimen. A surface-to-surface contact formulation was used. The boundary conditions were applied on the anvils, as shown in Fig. 1 (b). The low strain rate (10^{-3} s^{-1}) test was simulated in the Abaqus Standard, while the intermediate rate test (1 s^{-1}) was simulated using the Abaqus Explicit. For the low strain rate (10^{-3} s^{-1}) model, an enforced out-of-plane displacement that was equal to the experimental displacement at the damage onset [19] was applied to the upper anvil. For the intermediate strain rate (1 s^{-1}) model, a constant velocity was applied to the upper anvil using the instantaneous amplitude as defined in Abaqus.

3.2. Simulations of the high strain rate tests (10^3 s^{-1})

The SHPB tests were modelled using the Abaqus Explicit, where the entire model consisted of three elastic aluminium bars, i.e. incident, transmitted and striker bars, with the Young's modulus of 70.2 GPa, Poisson's ratio of 0.3, and density of 2720 kg/m^3. The incident and transmitted bars had a length of 1800 mm and a diameter of 11.95 mm. Likewise, the striker had the same diameter and a length of 300 mm. Several mesh densities were tested and, finally, an optimal element size of 0.5 mm was used for the cross-section of the bars. In order to obtain accurate results with a minimum computation time, the incident and transmitted bars were meshed with C3D8 elements using an element size that changed gradually from 0.3 mm in the contacts between the bars and specimen surfaces to 3 mm at the strain gauge locations, and up to 6 mm at the ends of bars. A surface-to-surface contact was used between the interfaces of the striker, incident bar, specimen, and transmitted bar. The penalty contact with the default hard contact formulation was applied in the tangential and normal directions, whereas the kinematic contact algorithm was used to allow the small sliding conditions.

The boundary conditions were set as shown in Fig. 2. The initial velocity of the striker was input using a predefined velocity field. The impact speed for each test was obtained from the experimental incident stress pulse (σ_i) using the equation: $\sigma_i = \frac{1}{2}\rho C_b V_0$. Here, C_b is the speed of the elastic stress (strain) pulse in the bar, which was obtained from $C_b = \sqrt{\frac{E_b}{\rho}}$. E_b and ρ are the Young's modulus and density of the bars, respectively.

3.3. Simulations of experimentally observed crack onset and growth

The VCCT crack propagation was modelled based on the crack plane observed in the in-situ high speed images of the experiments [19]. In the simulations, one crack plane was modelled to evaluate the effects of a brittle fracture on the force response. The pre-existing crack (or flaw) with a length of 0.3 mm was created at the interface of the plies with different fiber orientations. The crack plane was located diagonally in the YZ plane allowing the crack to propagate towards the surface, which was in contact with the anvil/bar, as shown in Fig. 3 (a). The critical ERR (G_C) of the crack propagation was determined according to the maximum G_{II} value of the damage onset point; the G_C value was estimated to be 285 J/m^2 for the tested specimen at the strain rate of 10^{-3} s^{-1}. For crack propagation, the enforced displacement was increased to 0.3 mm, which was equal to the experimental displacement at the peak force. In the dynamic (explicit) simulations, a range of G_C values was used to analyze how the critical ERR affects the force response at the high strain rate, as there is currently no standard method available for experimental determination of the high strain rate mode II fracture toughness [26].

For the static and dynamic simulations, multiple pre-cracks were modelled to study the effects of multiple weak points on the mechanical response. For the low strain rate (10^{-3} s^{-1}) model, the second pre-crack had a length of 0.4 mm and it was positioned at the surface of the crack plane in contact with the anvil (see Fig. 3 (b)). Moreover, a third internal pre-crack, with a length of 0.4 mm, was located in the middle of the crack plane (Fig. 3 (c)). For the high strain rate (10^3 s^{-1}) model, the second and third pre-cracks were 0.5 mm long (length is based on the real test specimen).

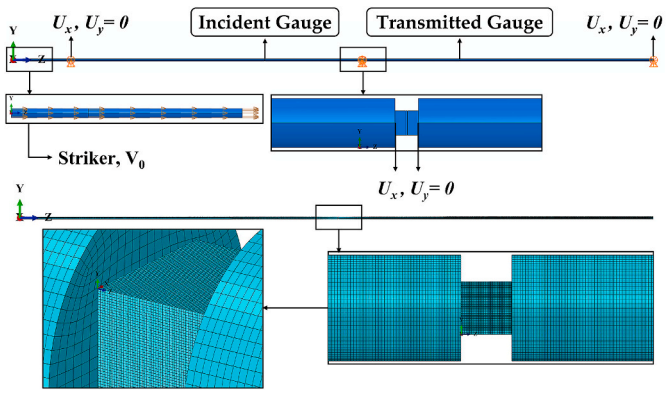

Fig. 2. The boundary conditions, loading, and element mesh used in the simulation of the high strain rate compression tests (SHPB).

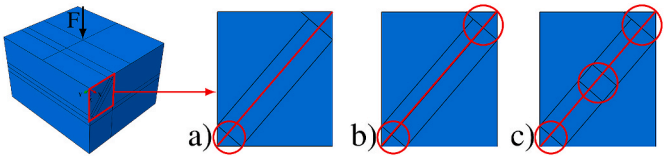

Fig. 3. The crack path with a) one pre-crack, b) two pre-cracks, and c) three pre-cracks. The crack and pre-cracks tip were marked with the red line and circles. (For interpretation of the references to colour in this figure legend, the reader is referred to the Web version of this article.)

4. Results

4.1. Predicted failure force and strain compared to the experimental data

Fig. 4 shows the experimental [19] and simulated force-strain responses of individual specimens at the low and intermediate strain rates. The simulated stiffnesses were mainly reproduced based on the experimental out-of-plane moduli and agreed with the experiments before any nonlinearity. The Poisson's ratio value ($\nu_{23} = 0.3$ and $\nu_{23} = 0.4$) had negligible effects on the predicted failure force and strain, as well as the failure mode and location (see supplementary data). The nonlinearity point in each curve was determined by plotting a line in the experimental force-strain data with the same slope as the Young's modulus and observing where the experimental data differs from the calculated line. The nonlinearity point was indicated by letters 'NL' in Fig. 4 (b). The simulated and experimental [19] failure onset points were indicated by the letters 'F' and 'D', respectively, in Fig. 4 (a). The 3DH criterion predicted clearly lower failure strains and force levels compared with the experimental damage onset when the crack was visible on the surface of the specimen. It suggests that the 3DH criterion merely predicted a phenomenon related to the earlier damage onset, e.g. micro-cracking and matrix damage. The experimental data might also be affected by geometric imperfections of the specimen. It is interesting to know how close the predicted failure onset was from either the nonlinearity point or the experimental damage onset point.

The strain and force of each specimen at the simulated failure point, the experimental damage onset point, and the nonlinearity point are presented in Table 2 and supplementary data to compare the predicted failure onset level precisely with the experimental data. Table 2 shows the relative difference between the simulated force at failure onset and the experimental force at the damage onset point (normalized with the experimental peak force), i.e. $\frac{(F_{IFF}-F_D)}{F_{peak}}$, as well as the difference between the simulated strain at failure onset and the experimental strain at the damage onset point (normalized with the experimental strain at the peak force), i.e. $\frac{(\varepsilon_{IFF}-\varepsilon_D)}{\varepsilon_{peak}}$. Likewise, Table 2 shows the difference between the simulated force at the failure onset and the experimental force at the nonlinearity point (normalized with the experimental peak force), i.e. $\frac{(F_{IFF}-F_{NL})}{F_{peak}}$, and also the difference between the simulated strain at failure onset and the experimental strain at the nonlinearity point (normalized with the experimental strain at the peak force), i.e. $\frac{(\varepsilon_{IFF}-\varepsilon_{NL})}{\varepsilon_{peak}}$. Clearly, the failure onset point predicted by the 3DH criterion matched better with the experimental nonlinearity point than the damage onset point not to mention the peak force or strain.

Table 2
The FEA predictions of compressive failure in this study.

Strain rate & specimen	ε_{IFF}[a] (mm/mm)	$\Delta\varepsilon_D$ (%)	F_{IFF}[a] (kN)	ΔF_D (%)	$\Delta\varepsilon_{NL}$ (%)	ΔF_{NL} (%)
Low (10^{-3} s^{-1}):						
SP1	0.016[b]	−39	4.9	−44	+6	+18
SP2	0.016[b]	−55	2.4	−40	+2	+16
Intermediate (1 s^{-1}):						
SP3	0.008[b]	−72	4.4	−58	−7	−3
High (10^3 s^{-1}):						
SP4	0.006[b]	−86	3.4[c]	−16	*N/A*	*N/A*
SP5	0.0055[b]	−140	5.7[c]	−18	*N/A*	*N/A*

[a] Stands for the load level when IFF reaches value of 1.
[b] Stands for the average strain computed over the specimen surface (YZ plane).
[c] Stands for the specimen failure force computed from the transmitted strain gauge signal.

4.2. Prediction of the location of failure in the low strain rate compression

Figs. 5 and 6 present the out-of-plane stress field and the failure mode at the damage onset (unity by criterion) at the strain rate of 10^{-3} s^{-1}. Fig. 5 (a) shows that the compressive stress (σ_{33}) in the middle ply was higher than the stresses in the upper and lower plies with the 0° fiber direction. The high IFF values were mainly due to the high σ_{33} stress component, which was higher than the in-plane stress components. The IFF failure onset occurred at the middle ply, in the XZ plane, close to the free edge, as highlighted in Fig. 6 (a). It can be also seen that the IFF mode remained low elsewhere. Interestingly, in the model with single elements through the ply thickness, the IFF mode shows the

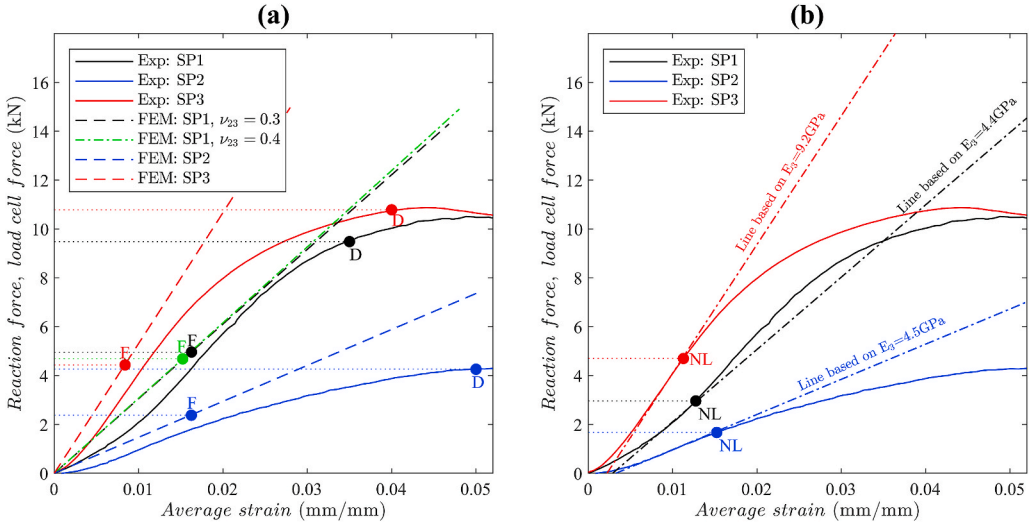

Fig. 4. The simulated and experimental [19] force-strain curves for the GFRP specimens under out-of-plane compression. (Note: (1) strain is the average strain computed over the specimen surface, YZ plane; (2) the FEA results were obtained with the model with dense mesh.).

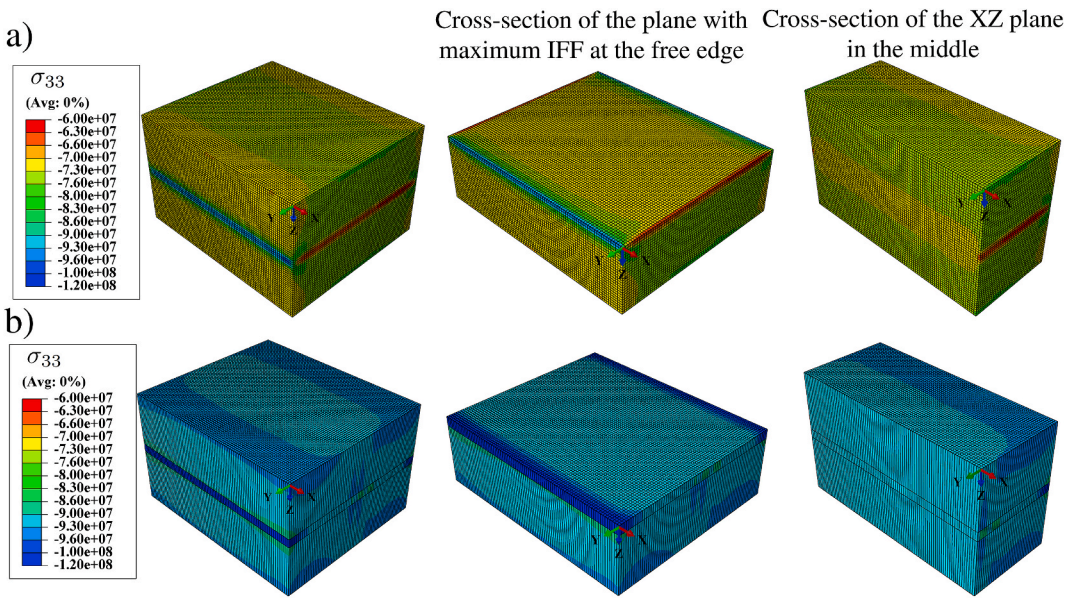

Fig. 5. The stress distributions at the predicted failure in the GFRP specimen (SP1) at the strain rate of 10^{-3} s^{-1} with (a) dense mesh; (b) mesh with single elements through thickness. The right-side images show the inside of specimen with the cross-section views.

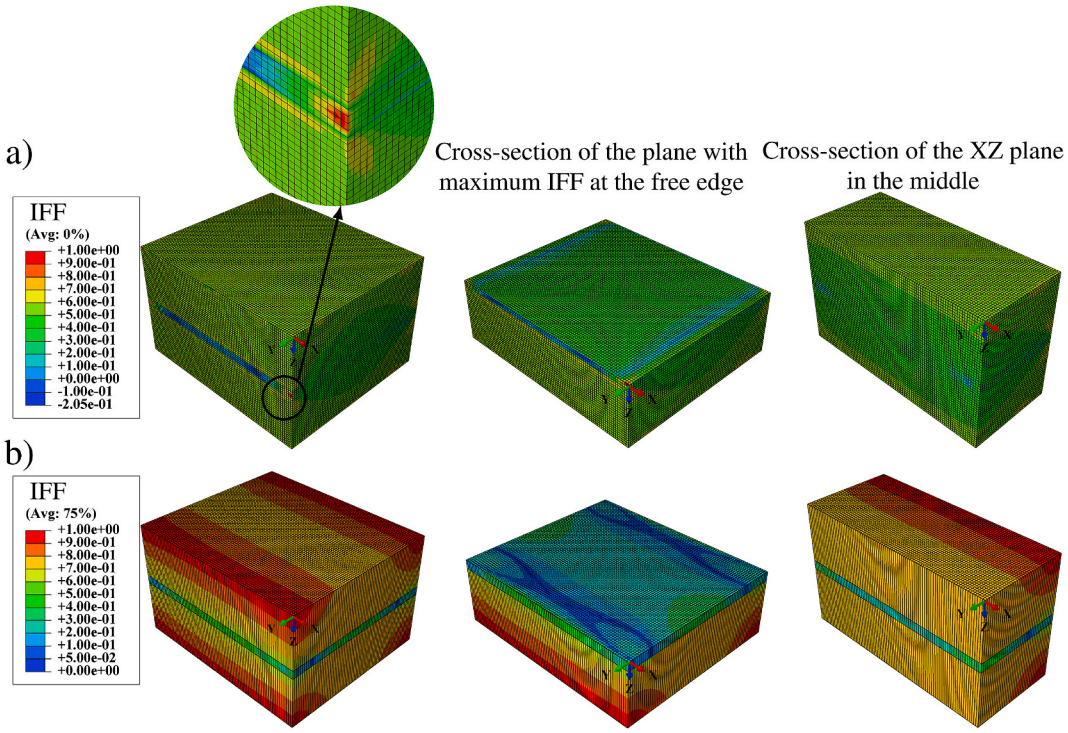

Fig. 6. The IFF mode at the predicted failure in the GFRP specimen (SP1) at the strain rate of 10^{-3} s^{-1} with (a) dense mesh; (b) mesh with single elements through thickness. The right-side images show the inside of specimen with the cross-section views.

highest values at the edges of the specimen, while the values were close to zero in the middle ply (Fig. 6 (b)). In this case, the failure was predicted to occur at the free edges that are in contact with the test machine anvils. Overall, the FF mode had low values. If no other damage would exist, the fiber failure would occur at the ply interfaces according to the simulations with dense mesh.

4.3. Prediction of the location of failure in the high strain rate compression

Fig. 7 shows the experimental strain gauge data and the corresponding data obtained from the simulation of the SHPB test (i.e., with the specimen SP4). The simulated incident and transmitted strain data fit well with the experimental results up to the moment when the failure onset was predicted. The FEA predicted that the failure occurs by the IFF mode. Apparently, the failure onset was predicted to occur before the experimental [19] D point. The Poisson's ratio did not significantly

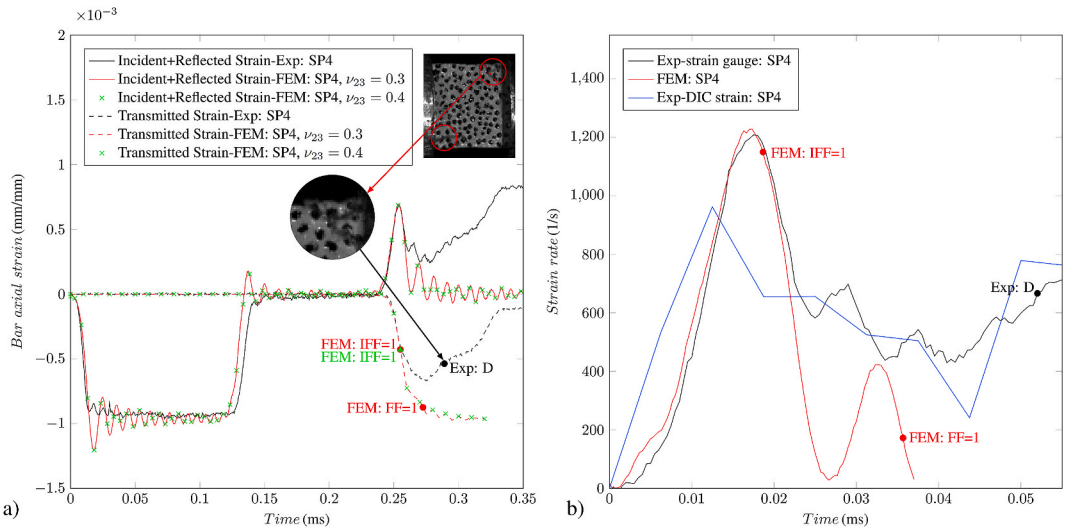

Fig. 7. The experimental and the corresponding FEA data for the high strain rate out-of-plane compression tests: (a) the strain gauge data; (b) the strain rate data of the specimen (SP4). The FEA results were obtained from the SHPB model with the dense mesh.

affect the simulated incident and transmitted strain data nor the failure onset prediction at the high strain rate (see supplementary data). Fig. 7 (b) shows the experimental and simulated strain rate data calculated using the reflected strain pulse. The 3DH criterion predicted the failure onset soon after the maximum strain rate that can be related to the micro-scale damage in the real specimen. However, the experimental macroscopic damage onset was observed when the load-carrying capability of the specimen drops and the strain rate increases. The strain rate was also obtained from the full field strains by calculating an average of the strain field over the surface of the specimen, and dividing the average strain by the time it took to reach the given frame. The nominal strain rate given for each compression experiment is the maximum strain rate obtained with DIC in the specimen before the damage onset.

The simulated stress field and failure mode for the high strain rate (10^3 s^{-1}) compression are shown in Figs. 8 and 9. The local compressive stresses were highest in the middle ply, on the specimen surface in the XZ plane. However, the cross-section views of the specimen show almost uniform stresses elsewhere inside the specimen. The predicted failure onset occurred predominantly due to the matrix cracking (i.e., IFF mode). The failure onset at the high strain rate was predicted at the middle ply on the specimen surface, as shown in Fig. 9. However, the failure onset in the specimen model with single elements through the ply was predicted at the edges that were in contact with bars, similarly as it was predicted by the low rate model. The FF mode had high values at the interfaces of the plies, which was related to the in-plane stress components. The comparison of the predicted failure for various strain rates demonstrates that the compressive stresses in the middle ply (on the XZ surface) in the high rate tests were higher than the stresses in the lower rate tests (at the failure location). The predicted first-occurring failure mode for both the low and the high strain rate simulations was the

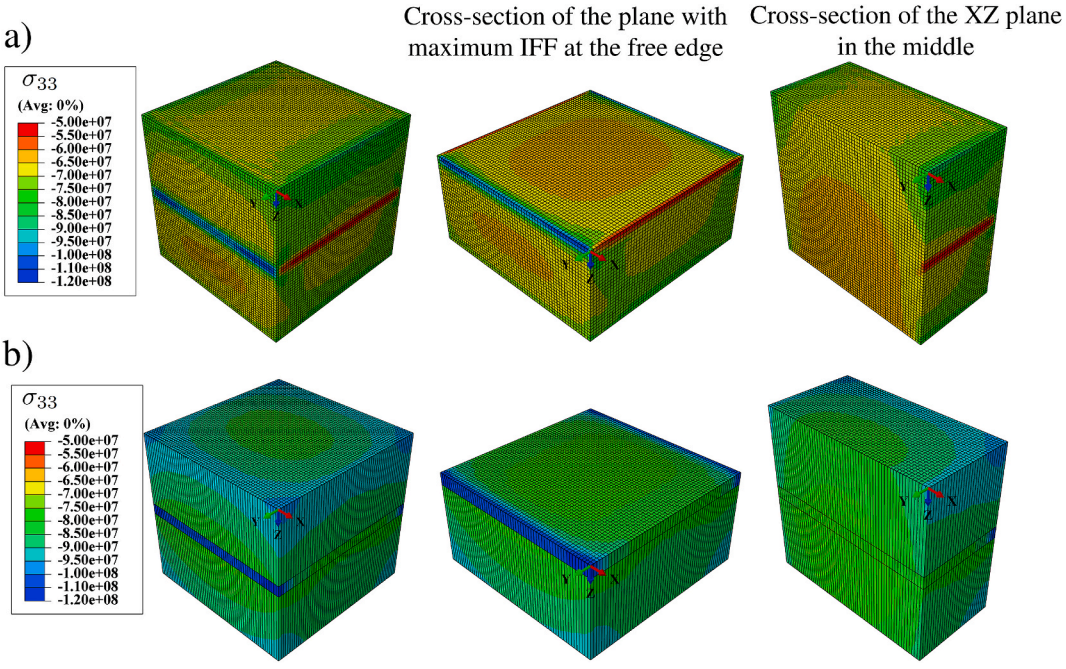

Fig. 8. The stress distributions at the predicted failure in the GFRP specimen (SP4) at the strain rate of 10^3 s^{-1} with (a) dense mesh; (b) mesh with single elements through thickness. The right-side images show the inside of specimen with the cross-section views.

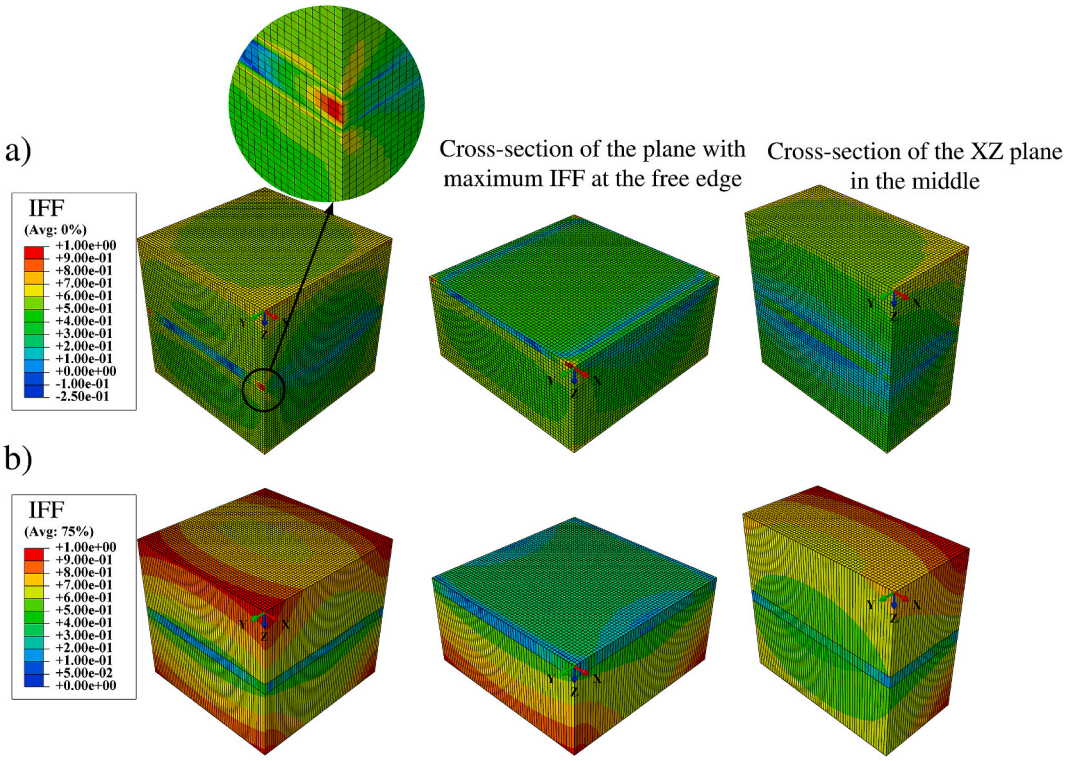

Fig. 9. The IFF mode at the predicted failure in the GFRP specimen (SP4) at the strain rate of 10^3 s^{-1} with (a) dense mesh; (b) mesh with single elements through thickness. The right-side images show the inside of specimen with the cross-section views.

compression matrix failure (i.e., IFF = 1) and this always occurred at the edges of the middle ply and on the XZ specimen surface.

4.4. The crack onset and propagation

The crack opening was observed by monitoring the compression experiments [19] with the high-speed optical and infrared cameras. The model with the VCCT focused only on simulating the crack onset. The simulated force-displacement curves of the model with the VCCT at the low strain rate (SP1) are shown in Fig. 10. The (reaction) force decreased sharply when the crack(s) propagated. The configuration of multiple pre-cracks (the modelled pre-flaws) had a negligible effect on the response (peak force). The bond state analysis by all the multiple pre-crack models indicates that the crack tip located at the free edge, and at the interface of plies, was the dominant failure point for crack propagation. Figs. 11 and 12 show the experimental strain gauge data and the corresponding data obtained from the simulation of the SHPB experiment (SP4). The simulated transmitted strains of the model with the VCCT crack propagation matched better with the experimental results prior to the peak force. Fig. 11 shows the incident and transmitted strain gauge data obtained from the crack-containing models with various G_C values. Apparently, the simulated amplitudes of the transmitted strain pulses increased when using lower G_C values than what was fitted based on the simulations for low rate testing (i.e. $G_C = 285$ J/m^2). However, the exact shape of the experimental pulses cannot be simulated using lower G_C values. Thus, it would be necessary to simulate exact material performance including the plasticity of the matrix polymer. In terms of the failure point, the VCCT can predict well the experimentally observed crack onset as long as the path/plane of the first crack was properly set. Fig. 12 compares the strain gauge data of the models with different pre-crack configurations. It is evident that the effects of multiple pre-cracks on the reflected and transmitted strain signals were negligible.

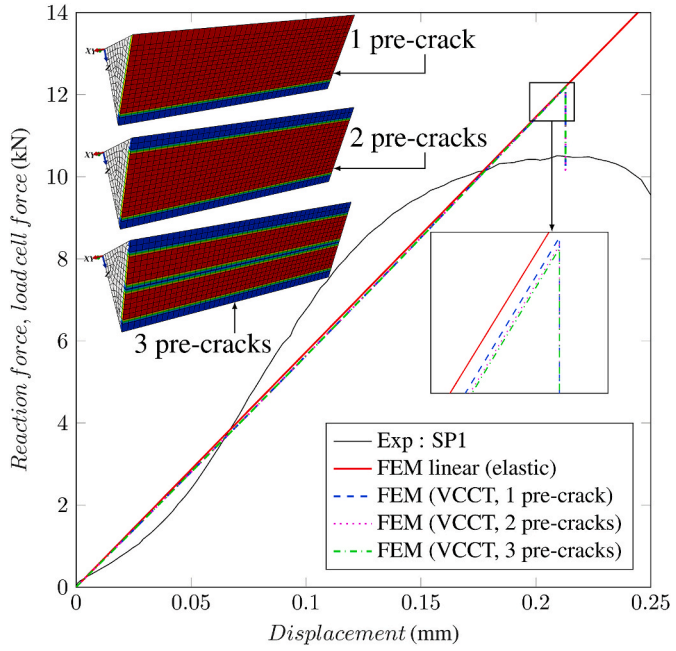

Fig. 10. The comparison of the experimental and simulated force-displacement curves for quasi-static out-of-plane compression with different patterns of pre-cracks and $G_C = 285$ J/m^2. The inset image shows the FEA-reported bond state illustration of the crack.

5. Discussion

Failure and especially its initiation in a composite laminate can occur locally and propagate rapidly [1,4,19]. In the experiments [19], the failure onset and crack propagation could only be observed on a single

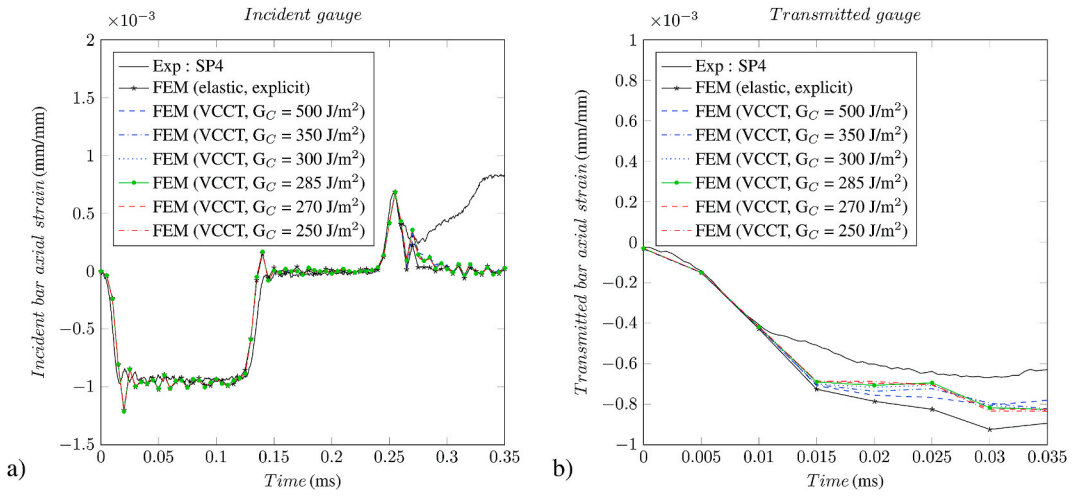

Fig. 11. The experimental strain gauge data and the corresponding FEA data for the high strain rate out-of-plane compression with different G_C values. The FEA results were obtained from the SHPB model with the dense mesh.

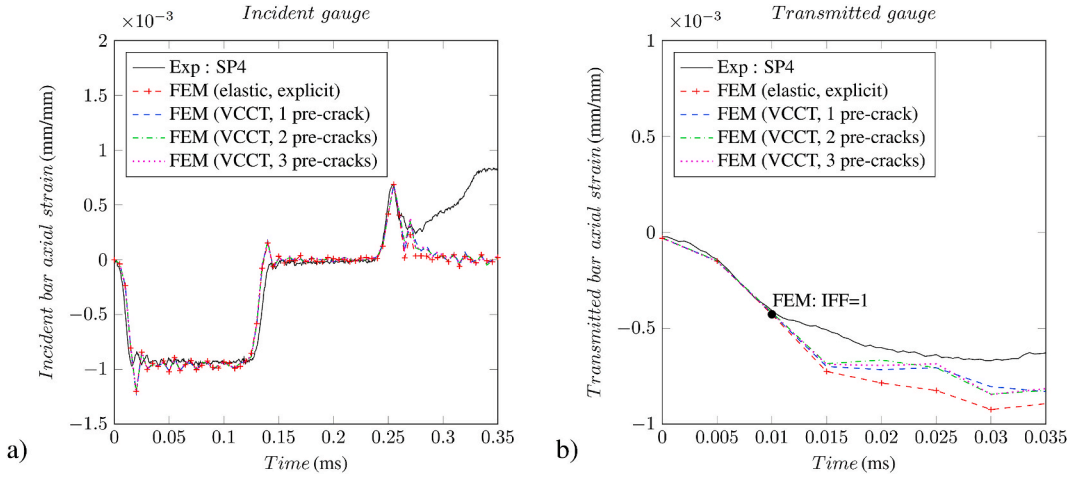

Fig. 12. The experimental strain gauge data and the corresponding FEA data for the high strain rate out-of-plane compression with different patterns of pre-cracks and $G_C = 300$ J/m^2. The FEA results were obtained from the SHPB model with the dense mesh.

specimen surface at a time. Based on the current FEA, the failure starts with compressive matrix failure, which is mainly caused by out-of-plane stresses. The mismatch of in-plane elastic properties between the plies with different orientations typically induces out-of-plane stress concentrations near free edges of the laminate [27,28]. Strictly speaking, the ply interfaces are prone to be locations of failure onset due to the concentrated occurrence of the stress field σ_{33} at free edges. Therefore, the location of failure was well predicted at the edges of the middle ply on the specimen surface. However, it should be noted that for the high rate tests, the specimens fracture fast into many fragments and, therefore, the location of (visual) damage and the timely order of failure processes should be analyzed with caution [3]. In general, the accuracy of predicted failure location by laminate plies is beneficial for design purposes.

Experimental compression data generally show significant nonlinearity [29,30] and it might be difficult to define a precise failure point. Furthermore, the out-of-plane compression behavior of composites is governed by the matrix behavior [31] that often shows plastic deformation or even some nonlinear elasticity. The nonlinear behavior can be also due to the geometric imperfections of the specimen, the dissipation, and the local temperature rise within shear bands [32,33]. Here, it was shown that the propagating (brittle) fracture cannot reproduce the nonlinear response prior to the peak force (stress). Thus, some microscopic damage is presumably taking place before the visual observation of the crack on the surface of the specimen, independent of the strain rate. Basically, validated nonlinear constitutive models [16] could help to model the plasticity within the crack propagation more precisely. For design purposes, fast and efficient failure criteria are necessary. This work has shown that the 3DH criterion predicts conservative failure loads, referring merely to the beginning of nonlinearity.

6. Conclusions

In this work, the mechanical failure of a GFRP laminate in out-of-plane compression at different strain rates was predicted using FEA and the 3DH criterion. The work focused on the prediction of the failure strain and force level, the failure mode including four different micro-scale modes, and the location of the failure in the lay-up. The simulation results were compared with the experimental data. The crack onset was simulated by the VCCT to better understand the specimen response and energy dissipation. The conclusions can be summarized as:

- The 3D Hashin criterion successfully predicted the location of failure onset at the middle ply on the outer surface of the specimen, where the crack opening was observed in the experiments [19] for low and intermediate strain rates loading. The predicted failure mode was

inter-fiber failure mainly due to the out-of-plane compressive stress component. The 3D Hashin criterion predicted lower failure strain and force values for each exact specimen model compared with the visual crack.

- The failure analysis of the GFRP specimens with a lay-up, under out-of-plane compression, required fine mesh (element size <25% ply thickness) to be able to predict the correct location of the failure onset in the lay-up.
- The simulations of fracture with VCCT could not precisely reproduce the nonlinear compressive response of the GFRP specimens prior to the peak force, thus, the plasticity-related dissipation or other damage might occur before the crack opening observed in reality.

Author contributions

Nazanin Pournoori. Writing-original draft, Writing-Review & editing, Methodology, Software, Validation, Formal analysis, Investigation, Visualization.

Oscar Rodera. Writing-Review & editing, Software, Formal analysis.

Jarno Jokinen. Writing-Review & editing, Software, Data curation.

Mikko Hokka. Writing-Review & editing, Supervision, Project administration.

Mikko Kanerva. Writing-Review & editing, Supervision, Conceptualization, Software, Project administration.

Declaration of competing interest

The authors declare that they have no known competing financial interests or personal relationships that could have appeared to influence the work reported in this paper.

Acknowledgement

This study was funded by a grant from Business Finland related to the 'LuxTurrim5G' (10098/31/2016) carried out by Tampere University and by a grant (5136/31/2019) of the SmartTram2 project. Also, a grant from Tampere University is acknowledged.

Appendix A. Supplementary data

Supplementary data to this article can be found online at https://doi.org/10.1016/j.compscitech.2021.109141.

References

[1] M. Tarfaoui, S. Choukri, A. Neme, Effect of fibre orientation on mechanical properties of the laminated polymer composites subjected to out-of-plane high strain rate compressive loadings, Compos. Sci. Technol. 68 (2) (2008) 477–485.
[2] M.M. Shokrieh, M.J. Omidi, Compressive response of glass–fiber reinforced polymeric composites to increasing compressive strain rates, Compos. Struct. 89 (4) (2009) 517–523.
[3] M.I. Okereke, C. Paul Buckley, A.I. Akpoyomare, The mechanism of rate-dependent off-axis compression of a low fibre volume fraction thermoplastic matrix composite, Compos. Struct. 168 (2017) 685–697.
[4] J. Arbaoui, M. Tarfaoui, A. El Malki Alaoui, Mechanical behavior and damage kinetics of woven E-glass/vinylester laminate composites under high strain rate dynamic compressive loading: experimental and numerical investigation, Int. J. Impact Eng. 87 (2016) 44–54.
[5] M. May, Measuring the rate-dependent mode I fracture toughness of composites – a review, Compos. Part A Appl. Sci. Manuf. 81 (2016) 1–12.
[6] M.J. Hinton, A.S. Kaddour, P.D. Soden, Failure Criteria in Fibre Reinforced Polymer Composites: the World-wide Failure Exercise, Elsevier Science and Technology, Oxford, 2004.
[7] A. Kaddour, M. Hinton, Challenging lessons from the second world-wide failure exercise (WWFE-II), in: Predicting Failure in Polymer Composite Laminates under 3-D States of Stress, 19th International Conference on Composite Materials, ICCM-19), Montreal, 2013.
[8] J. Gu, P. Chen, Some modifications of Hashin's failure criteria for unidirectional composite materials, Compos. Struct. 182 (2017) 143–152.
[9] Pinho, S.T., Dávila, C.G., Camanho, P.P., Iannucci, L., Robinson, P., Failure Models and Criteria for FRP Under-in-plane or Three-Dimensional Stress States Including Shear Non-linearity, Technical Report NASA/TM-2005-213530.
[10] A. Puck, H. Schürmann, Failure analysis of FRP laminates by means of physically based phenomenological models, Compos. Sci. Technol. 58 (7) (1998) 1045–1067.
[11] I.M. Daniel, B.T. Werner, J.S. Fenner, Strain-rate-dependent failure criteria for composites, Compos. Sci. Technol. 71 (3) (2011) 357–364.
[12] Y. Tao, H. Chen, K. Yao, H. Lei, Y. Pei, D. Fang, Experimental and theoretical studies on inter-fiber failure of unidirectional polymer-matrix composites under different strain rates, Int. J. Solid Struct. 113–114 (2017) 37–46.
[13] R.M. Guedes, M.F. de Moura, F.J. Ferreira, Failure analysis of quasi-isotropic CFRP laminates under high strain rate compression loading, Compos. Struct. 84 (4) (2008) 362–368.
[14] S. Eskandari, F.M. Andrade Pires, P.P. Camanho, H. Cui, N. Petrinic, A.T. Marques, Analyzing the failure and damage of FRP composite laminates under high strain rates considering visco-plasticity, Eng. Fail. Anal. 101 (2019) 257–273.
[15] B.T. Werner, I.M. Daniel, Characterization and modeling of polymeric matrix under multi-axial static and dynamic loading, Compos. Sci. Technol. 102 (2014) 113–119.
[16] S.V. Thiruppukuzhi, C. Sun, Models for the strain-rate-dependent behavior of polymer composites, Compos. Sci. Technol. 61 (1) (2001) 1–12.
[17] T. Mostapha, Experimental investigation of dynamic compression and damage kinetics of glass/epoxy laminated composites under high strain rate compression, in: Adv. Compos. Mater. - Ecodesign Anal, 2011, pp. 359–380.
[18] A. Kara, A. Tasdemirci, M. Guden, Modeling quasi-static and high strain rate deformation and failure behavior of a (±45) symmetric E-glass/polyester composite under compressive loading, Mater. Des. 49 (2013) 566–574.
[19] N. Pournoori, G. Corrêa Soares, O. Orell, S. Palola, M. Hokka, M. Kanerva, Adiabatic heating and damage onset in a pultruded glass fiber reinforced composite under compressive loading at different strain rates, Int. J. Impact Eng. 147 (2021) 103728.
[20] Z. Hashin, Failure criteria for unidirectional fiber composites, J. Appl. Mech. Trans. ASME. 47 (2) (1980) 329–334.
[21] Z. Hashin, A. Rotem, A fatigue failure criterion for fiber reinforced materials, J. Compos. Mater. 7 (4) (1973) 448–464.
[22] R. Krueger, Virtual crack closure technique: history, approach, and applications, Appl. Mech. Rev. 57 (2) (2004) 109–143, https://doi.org/10.1115/1.1595677.
[23] G. Ravichandran, G. Subhash, Critical appraisal of limiting strain rates for compression testing of ceramics in a split Hopkinson pressure bar, J. Am. Cerm. Soc. 77 (1) (1994) 263–267.
[24] P. Pei, Z. Pei, Z. Tang, Numerical and theoretical analysis of the inertia effects and interfacial friction in SHPB test systems, Materials 13 (21) (2020) 1–17, https://doi.org/10.3390/ma13214809.
[25] O. Rodera Garcia, Damage Onset Modelling of Curved Composite Laminates, Master's Thesis, Tampere University, Finland, 2018.
[26] M. May, H. Channammagari, P. Hahn, High-rate mode II fracture toughness testing of polymer matrix composites – a review, Compos. Part A Appl. Sci. Manuf. 137 (2020) 106019.
[27] C. Mittelstedt, W. Becker, Free-edge effects in composite laminates, Appl. Mech. Rev. 60 (5) (2007) 217–245.
[28] D. Post, B. Han, P. Ifju, Laminated composites in compression: free-edge effects, in: High Sensitivity Moiré, Springer, 1994, pp. 273–292.
[29] O. Allix, P. Ladevèze, E. Vittecoq, Modelling and identification of the mechanical behaviour of composite laminates in compression, Compos. Sci. Technol. 51 (1) (1994) 35–42.
[30] B.C. Ray, D. Rathore, A review on mechanical behavior of FRP composites at different loading speeds, Crit. Rev. Solid State Mater. Sci. 40 (2) (2015) 119–135, https://doi.org/10.1080/10408436.2014.940443.
[31] C. González, J. LLorca, Mechanical behavior of unidirectional fiber-reinforced polymers under transverse compression: microscopic mechanisms and modeling, Compos. Sci. Technol. 67 (13) (2007) 2795–2806.
[32] Z. Li, J. Lambros, Dynamic thermomechanical behavior of fiber reinforced composites, Compos. Part A Appl. Sci. Manuf. 31 (6) (2000) 537–547.
[33] M. Tarfaoui, A. El Moumen, H. Ben Yahia, Damage detection versus heat dissipation in E-glass/epoxy laminated composites under dynamic compression at high strain rate, Compos. Struct. 186 (2018) 50–61.